2017

Mechanistic Modeling of the Liquid Film Shape and Heat Transfer Coefficient in Annular-Regime Microchannel Flow Boiling

R. S. Patel
Purdue University

J. W. Weibel
Purdue University, jaweibel@purdue.edu

S. V. Garimella
Purdue University, sureshg@purdue.edu

Patel, R. S.; Weibel, J. W.; and Garimella, S. V., "Mechanistic Modeling of the Liquid Film Shape and Heat Transfer Coefficient in Annular-Regime Microchannel Flow Boiling" (2017). *CTRC Research Publications.* Paper 317.
http://dx.doi.org/http://dx.doi.org/10.1016/j.ijheatmasstransfer.2017.06.121

Mechanistic Modeling of the Liquid Film Shape and Heat Transfer Coefficient in Annular-Regime Microchannel Flow Boiling

Ravi S. Patel, Justin A. Weibel, and Suresh V. Garimella[1]

Cooling Technologies Research Center, an NSF IUCRC

School of Mechanical Engineering and Birck Nanotechnology Center

Purdue University, West Lafayette, IN 47907-2088 USA

ABSTRACT

A methodology is proposed for predictive modeling of the liquid-gas interface shape and saturated flow boiling heat transfer coefficient in two-phase microchannel flows within the annular regime. The mechanistic model accounts for the effects of surface tension and interface curvature, gravity, and shear stress in determining the liquid film shape; one-dimensional conduction is assumed to occur across the variable-thickness film to calculate wall heat transfer coefficients locally along the channel length. Model performance is benchmarked against 251 experimentally measured heat transfer coefficient values taken from the literature for annular-regime flow boiling in microchannels of a rectangular cross-section. These data are successfully predicted with a mean absolute error of 21.7%, and 72.1% of the points lie within an error band of ±30%. The match to data is poorest at lower vapor qualities corresponding to the onset of the annular regime, for which the heat transfer coefficient is underpredicted; an experimental investigation is performed to better understand the disparity under these operating conditions. Liquid film shapes are measured during adiabatic annular flow through microchannels of square cross-section for a range of channel hydraulic diameters (160 μm, 510 μm, 1020 μm) and operating conditions, so as to control the void fraction and Weber number of the flow. Using air and water as the working gas and liquid, respectively, trends in film behavior are identified and

---

[1] Author to whom correspondence should be addressed: (765) 494-6209, sureshg@purdue.edu

compared against model predictions. The experimental findings reveal the non-negligible impact of capillary pumping on the interface morphology at the onset of the annular regime.

Keywords

two-phase microchannel flow; annular regime; mechanistic model; heat transfer performance; liquid film thickness

Nomenclature

A	area, m^{2}
c_p	specific heat capacity, J kg^{-1} K^{-1}
D_f	depth of field, m
D_h	hydraulic diameter, m
e	camera resolution, m
f_i	friction factor
G	fluid mass flux, kg m^{-2} s^{-2}
g	gravitational acceleration, m s^{-2}
h	heat transfer coefficient, W m^{-2} K^{-1}
h_{fg}	latent heat of vaporization, J kg^{-1}
j	superficial phase velocity, m s^{-2}
k	thermal conductivity, W m^{-1} K^{-1}
L_{a0}	streamwise location of onset of annular flow regime, m
M	magnification
m	mass flow rate, kg s^{-1}
m_z	streamwise mass flow rate, kg rad^{-1} s^{-1}
m_θ	angular mass flow rate, kg m^{-1} s^{-1}
n	index of refraction
NA	numerical aperture
Nu	Nusselt number (hD_h/k)
O	polar coordinate system origin
p	pressure, Pa
P_c	vapor core pressure, Pa
P_H	heated perimeter, m
q''	heat flux, W m^{-2}
r	radial position, m
r_c	radius of curvature, m
S	perimeter, m
T	temperature, K

u	velocity, m s^{-1}
We	Weber number ($\rho u^2 D_H/\sigma$)
x	spanwise coordinate position, m
$\hat{x}$	normalized spanwise coordinate position
x_e	thermodynamic vapor quality
x_f	flow quality
y	depth coordinate position, m
$\hat{y}$	normalized depth coordinate position
z	streamwise coordinate position, m

Greek Symbols

α	volumetric void fraction
δ	film thickness, m
η	interface evolution parameter, s
θ	angular position, rad
λ	wavelength, m
μ	dynamic viscosity, kg m^{-1} s^{-1}
ρ	density, kg m^{-3}
σ	surface tension, N m^{-1}
τ_i	interfacial shear stress, Pa
φ	volume fraction

Subscripts

cs	cross-sectional
exp	experimentally observed
f	liquid phase
g	gas phase
i	interface
in	inlet
$pred$	model-predicted
sat	saturated liquid
w	wall
z	streamwise component
θ	angular component

1 INTRODUCTION

Multiphase flows through small-scale channels are encountered across a wide range of applications. Technologies that leverage the enhanced transport behavior at small scales to extend their performance envelopes include fuel cells that are able to achieve higher efficiencies and power densities [1], chemical reactors that have greater mass transfer and reaction rates leading to higher yields and/or smaller system sizes [2], and high-performance compact heat exchangers [3]. In particular, two-phase microchannel heat sinks are an attractive option for the thermal management of electronic devices, capable of removing high heat fluxes while maintaining uniformity in device surface temperatures; however two-phase operation is not widely employed due to difficulties associated with performance prediction [4].

Traditional correlation-based performance prediction methodologies fit functions to experimental data. The utility of these empirical fits is inherently restricted to the conditions under which they were developed [5]; therefore, a broad range of design parameters, such as channel dimensions and coolant flow rates must be incorporated into the fitting to broaden the applicable range. Bertsch *et al.* [5] performed a comprehensive review and analysis of a wide range of correlations developed for macro- and micro-scale flow boiling. They observed that the best predictions had a mean absolute error (MAE) of 40% when compared to experiments, with less than half of the data points being predicted within an error band of ±30%. Furthermore, it was observed that the pool boiling correlations of Cooper [6] and Gorenflo [7] both outperformed all flow boiling correlations considered in that study. These findings highlighted the need to develop mechanistic performance models grounded in the underlying physics of microscale flow boiling, rather than a continued effort to refine correlations that are based on empirical inputs [5].

The annular flow regime, characterized by a continuous vapor core surrounded by a liquid film on the channel walls, is of particular interest when considering small-scale channels as it is one of the more commonly encountered flow morphologies [8]. Researchers have attempted to develop predictive tools specific to this annular flow regime that capture the underlying mechanics of the flow, rather than relying purely on empirical observations. Qu and

Mudawar [9] developed a simplified analytical model of annular-regime microchannel flows by assuming that evaporation from the thin liquid film was the predominant heat transfer mechanism. As a simplifying assumption, the model treated the film as having a uniform thickness around the inside perimeter of the channel, with the heat transfer coefficient being calculated as the inverse of the conduction thermal resistance across this film. Starting with a guess for the film thickness, the streamwise pressure gradient was found using a momentum balance within the liquid film. Next, a momentum balance within the vapor core allowed for the interfacial shear stress to be found using the computed pressure gradient. Finally, a friction factor approach was used to calculate an alternate value for the interfacial shear stress and the two uniquely determined shear stress values are compared. The film thickness was iterated using these solution steps until a value was found that allowed matching of these two interfacial shear stresses, and the procedure was repeated at subsequent downstream computational elements. When benchmarked against experimental data obtained in a copper microchannel heat sink having channels with a 231 μm × 713 μm cross-section using water as the working fluid [10], this model achieved an MAE of 13.3% in predicting heat transfer coefficient, with all data located within an error band of ±40% [9]. To achieve the quoted accuracy, the model included an empirical correlation fitted to the data set used; this correlation was incorporated into the model as a mass transfer term to account for liquid deposition into the film from entrained droplets [9].

This modeling process was modified by Harirchian and Garimella [11], who again treated the film as having a uniform thickness within the channel cross-section at each streamwise location. An improved solution procedure was developed by calculating the pressure gradient from a momentum balance in the streamwise direction for the vapor core, rather than the liquid film. Interfacial shear stress was found using a friction factor approach, and together with the pressure drop, was used to find the liquid mass flow rate. A direct relationship was thereby established between film thickness and mass flow rate. The film thickness could then be readily iterated until the calculated mass flow rate matched the known flow rate. This solution strategy decreased the sensitivity of model convergence to the film thickness and choice of increment size in film thickness changes, thus yielding a more robust numerical procedure [11] compared to the model of Qu and Mudawar [9]. The model was benchmarked against experimental heat transfer coefficient measurements resulting in an MAE of 17.3% with 82.2% of predictions within ±30% for confined annular flows, and an MAE of 21.8% with 78.0% of predictions within ±30% for annular/wispy annular flows [11]. A large dataset of experimental results was obtained in silicon microchannel heat sinks with channel widths ranging from 100 to 5850 μm and depths ranging from 100 to 400 μm, using FC-77 as the working fluid [12,13]. The model again used the empirical correlation for mass deposition into the liquid film from entrained droplets [9], and also introduced an empirically fitted correction to the interfacial friction factor [11].

Jesseela and Sobhan [4] recently developed a model for annular two-phase microchannel flows that took into account effects of surface tension on pressure within the individual phases locally along the length of the channel. A solution procedure similar to Harirchian and Garimella [11] was adopted with an additional step to calculate the local pressure and streamwise pressure gradients within the liquid film and the vapor core individually. The Young-Laplace relation was used to find the radius of curvature of the liquid-gas interface that resulted from the pressure differential across the interface. Despite calculating interface curvature, the heat transfer coefficient was predicted assuming a conformal film of uniform thickness within the channel cross-section; interface curvature was only used in determining pressure-related information. Key trends generated by the model were presented and discussed [4], but the model was not comprehensively benchmarked against experimental data.

The present work seeks to expand upon the existing physics-based models of annular microchannel flows by capturing the film shape in greater detail and, thereby, reduce the dependence of the model on empirical inputs. The traditional assumption of a uniform film thickness within the channel cross-section is relaxed. A two-dimensional liquid-gas interface shape is analytically determined by including the effects of gravity and surface tension, in addition to the effects of shear stress that were accounted for in previous models. Aside from the friction factor relation used to calculate interfacial shear stress, no empirical inputs are included in the model formulation; there is no fitting of empirical factors to improve model performance. The model-predicted heat transfer coefficients are benchmarked against experimental heat transfer data from a wide range of sources in the literature. An experimental parametric investigation of the effects of channel size and operating conditions on liquid-gas interface shape is conducted, using a measurement technique developed by the authors in a previous study [14], to investigate specific conditions under which the model performance deviates from experimental observations.

2 MODEL DEVELOPMENT

2.1 Liquid Film Profile in Annular Two-Phase Flow

An annular flow boiling model is developed that captures the two-dimensional liquid film profile within the channel cross-section, as well as the evolution of this profile in the streamwise direction. A similar approach was presented by Wang and Rose [15], but for condensing flows. The effects of surface tension at the curved interface, gravity, and momentum diffusion in both phases are taken into account, while the effects of momentum advection are neglected based on a Stokes flow assumption due to the very small film thicknesses considered. The cylindrical coordinate system shown in Figure 1 is adopted to describe the flow, wherein the origin *O* is located at the centroid of the rectangular channel cross-section at the channel inlet and the *z* axis extends in the streamwise direction. The film thickness δ is taken as the distance from the channel wall to the liquid-gas interface along the radial direction relative to the origin *O*. While rectangular channels are investigated in the present work, the model is applicable to channels of arbitrary cross-sectional shape.

Assuming an incompressible, steady-state, and fully developed flow of a Newtonian fluid, the θ- and *z*-components, respectively, of the momentum equations for the liquid film are

$$\mu_f \frac{\partial}{\partial r}\left(\frac{1}{r}\frac{\partial}{\partial r}\left(r u_\theta\right)\right)+\left(\rho_f-\rho_g\right) g sin\left(\theta\right)=\frac{1}{r}\frac{\partial p}{\partial \theta} \tag{1}$$

$$\mu_f \left(\frac{1}{r}\frac{\partial}{\partial r}\left(r\frac{\partial u_z}{\partial r}\right)\right)=\frac{dp_c}{dz} \tag{2}$$

In Eq. (1), $\partial p/\partial \theta$ represents the pressure gradient in the circumferential direction induced within the cross-section of the liquid film due to changes in the curvature of the liquid-gas interface. In Eq. (2), dp_c/dz is the pressure gradient within the vapor core, as it is assumed that the streamwise pressure gradient within the liquid film is the same as that in the vapor core. The circumferential pressure gradient is found by differentiating the Young-Laplace relation as follows.

$$\frac{\partial p}{\partial \theta}=-\sigma\frac{\partial}{\partial \theta}\left(\frac{1}{r_c}\right) \tag{3}$$

In Eq. (3), r_c is the local radius of curvature of the interface calculated as

$$\frac{1}{r_c} = \frac{r_i^2 + 2(\partial r_i / \partial \theta)^2 - r_i(\partial^2 r_i / \partial \theta^2)}{\left\{ r_i^2 + (\partial r_i / \partial \theta)^2 \right\}^{3/2}} \tag{4}$$

The streamwise pressure drop, $\partial p_c/\partial z$, is obtained from a momentum balance within the core for one-dimensional vapor flow. As a simplification, the model assumes that the pressure within the liquid and gas phases are identical at any given streamwise location, and does not take into account any streamwise change in interface curvature or consider the implications of the increase in pressure on the vapor-side of the interface that arises from the curvature:

$$\frac{dp_c}{dz} + \frac{\rho_g}{A_g}\frac{d}{dz}\left(u_g^2 A_g\right) + \frac{\tau_i S_i}{A_g} = 0 \tag{5}$$

In Eq. (5), τ_i is the interfacial shear stress between the liquid film and the vapor core, and is found using an annular-flow friction factor correlation developed by Moeck [16] using an air-water system. The interfacial shear stress and the friction factor are calculated as

$$\tau_i = \frac{1}{2} f_i \rho_g u_g^2 \tag{6}$$

$$\text{where } \; f_i = 0.005\left[1 + 1458\left(\frac{\delta}{D_h}\right)^{1.42}\right] \tag{7}$$

The velocity of the vapor core is

$$u_g = \frac{\dot{m}_g}{\rho_g A_g} \tag{8}$$

The vapor and liquid mass flow rates are found as

$$\dot{m}_g = x_e G A_{cs} \tag{9}$$

$$\dot{m}_f = (x_e - 1) G A_{cs} \tag{10}$$

where the thermodynamic vapor quality is found using an energy balance.

$$x_e = \frac{1}{h_{fg}}\left[\frac{q_w'' P_H z}{G A_{cs}} - c_p\left(T_{sat} - T_{in}\right)\right] \tag{11}$$

Eq. (1) and (2) are solved by integration across the liquid film in the *r*-direction from the liquid-gas interface to the channel wall, subject to a no-slip boundary condition at the channel wall in the *z* and *θ* directions, a no-shear condition for the liquid-gas interface in the *θ* direction, and an interfacial shear stress condition in the streamwise direction, as respectively defined below.

$$u_z = u_\theta = 0 \quad \text{at} \quad r = r_w \tag{12}$$

$$\frac{\partial u_\theta}{\partial r} = 0 \quad \text{at} \quad r = r_i \tag{13}$$

$$-\frac{1}{\mu_f}\frac{\partial u_z}{\partial r} = \tau_i \quad \text{at} \quad r = r_i \tag{14}$$

The resulting velocity profiles within the liquid film are

$$\begin{aligned} u_\theta = \frac{1}{6\mu_f\left(r_i^2 + r_w^2\right) r}\Bigg[& 3\sigma\frac{\partial}{\partial\theta}\left(\frac{1}{r_c}\right)\Big(r_i^2\left(r^2 - r_w^2\right)\ln\left(r_i\right) + \\ & r_w^2\left(r^2 + r_i^2\right)\ln\left(r_w\right) - r^2\left(r_i^2 + r_w^2\right)\ln\left(r\right) + r_i^2\left(r^2 - r_w^2\right)\Big) \\ & -2g\left(\rho_f - \rho_g\right)\sin\left(\theta\right)\left(r - r_w\right)\Big(\left(-2r - 2r_w\right)r_i^3 + \\ & \left(r^2 + r r_w + r_w^2\right)r_i^2 + r^2 r_w^2\Big) \Bigg] \end{aligned} \tag{15}$$

$$u_z = \frac{1}{4\mu_f}\frac{dp_c}{dz}\left(-2\ln\left(\frac{r}{r_w}\right)r_i^2 + r^2 - r_w^2\right) - \frac{\tau_i r_i}{\mu}\left(\ln\left(\frac{r}{r_w}\right)\right) \tag{16}$$

Next, by integrating Eq. (15) across the liquid film in the *r* direction, the liquid mass flow rate in the circumferential direction is calculated (per unit length in the streamwise direction). Similarly, by integrating Eq. (16) across the liquid film, the streamwise mass flow rate per radian can be found.

$$m_\theta = \int_{r_i}^{r_w} \rho_f u_\theta dr =$$

$$\frac{\rho_f g}{\mu_f} f_g(\delta)\left(\rho_f - \rho_g\right)\sin(\theta) + f_s(\delta)\frac{\rho_f \sigma}{\mu_f}\frac{\partial}{\partial \theta}\left(\frac{1}{r_c}\right) \tag{17}$$

$$m_z = \int_{r_i}^{r_w} r \rho_f u_z dr = \frac{\rho_f}{\mu_f} f_z(\delta)\frac{dp_c}{dz} + f_\tau(\delta)\frac{\rho_f}{\mu_f}\tau_i \tag{18}$$

where $f_g(\delta)$, $f_s(\delta)$, $f_z(\delta)$, and $f_\tau(\delta)$ are functions of the local film thickness δ corresponding to the buoyancy, surface tension, streamwise pressure gradient, and interfacial shear stress terms, respectively, and are defined in Appendix A.

Conservation of mass can then be applied to the liquid film cross-section to find the response of the film thickness δ to circumferential flow within the film.

$$\frac{\partial \delta}{\partial \eta} = -\frac{1}{\rho_f r_i}\frac{\partial m_\theta}{\partial \theta} \tag{19}$$

In Eq. (19) the evolution parameter η enables determination of the steady-state liquid film cross-sectional shape from an initial estimate. Finally, substituting Eq. (17) into Eq. (19) yields a differential equation in terms of the unknown variable δ, which is discretized and solved iteratively until the liquid film cross-section achieves a steady state in the evolution parameter η.

$$\begin{aligned}\frac{\partial \delta}{\partial \eta} = &-\frac{\left(\rho_f - \rho_g\right)}{\mu_f}\frac{g}{r_i}\frac{\partial}{\partial \theta}\left(f_g(\delta)\sin(\theta)\right) \\ &-\frac{\sigma}{\mu_f r_i}\frac{\partial}{\partial \theta}\left(f_s(\delta)\frac{\partial}{\partial \theta}\left(\frac{1}{r_c}\right)\right)\end{aligned} \tag{20}$$

Eq. (20) is subject to the boundary condition $\partial\delta/\partial\theta = 0$ at $\theta = 0$ and 2π, assuming that the profile is smooth and continuous.

2.2 Heat Transfer Coefficient

Heat transfer is modeled assuming one-dimensional conduction from the channel wall to the evaporating liquid-gas interface, where the interfacial evaporation resistance is negligible. As a result, the heat transfer coefficient can be locally calculated as the inverse of the conduction thermal resistance across the local film thickness along the perimeter of the channel.

$$h_{w,local} = \frac{-k_f}{r_w \ln\left(\frac{r_w - \delta}{r_w}\right)} \tag{21}$$

The simplification of one-dimensional radial heat transfer, as applied to a two-dimensional liquid film shape, can potentially lead to an underprediction of heat transfer coefficient under certain conditions, namely when the channel aspect ratio is very high or the liquid film is highly conformal to the channel walls. In the current study, this disparity is shown to be negligible for the comparisons made here to experimental heat transfer coefficient data in rectangular microchannels with aspect ratios up to 3:1, across a wide range of operating conditions.

As has been done in previous studies [11,17], a dryout condition is implemented whereby heat is assumed to be transferred directly to the vapor phase when the liquid film is thinner than the surface roughness of the channel walls. The single-phase heat transfer coefficient in dried-out regions of the wall is calculated based on the average Nusselt number for the appropriate channel geometry assuming fully developed laminar flow in the vapor core. The overall heat transfer coefficient for the heat sink at a given streamwise location is then found by taking an area-weighted average of the local wall heat transfer coefficient over the heated perimeter of the channel.

$$h_{pred} = \frac{\int_{P_H} h_{w,local}\, dP_H}{P_H} \tag{22}$$

2.3 Solution Procedure

The steady-state solution for the liquid film cross-section given in Eq. (20) is found using an iterative approach by starting with a guess for the initial film thickness δ and subsequently updating the film shape until a converged solution is found. This equation is solved numerically by discretizing the channel into a uniformly spaced grid in both the θ and z directions. The following solution procedure is initiated at the streamwise location that corresponds to the onset of the annular flow regime, L_{a0}, which can be found using the methodology proposed by Harirchian and Garimella [11].

1. At the first streamwise node the initial guess for the interface profile is taken as a conformal film with uniform thickness around the perimeter of the channel. At subsequent downstream nodes the guess is taken as the interface profile calculated at the previous streamwise node to accelerate the solution procedure.
2. Starting with the guess, Eq. (20) is solved using a forward-time, center-space explicit scheme to obtain the $\partial\delta/\partial\eta$ term. The derivative of δ with respect to the evolution parameter η is used to update the liquid film cross-section, and the calculation is repeated with the updated interface profile until a converged solution for δ is obtained (*i.e.*, $\partial\delta/\partial\eta \approx 0$).
3. Once the interface profile is found, the friction factor is determined using Eq. (7), the resulting interfacial shear stress using Eq. (6), and the streamwise pressure gradient using

Eq. (5).

4. This yields all terms necessary to calculate the streamwise liquid mass flow rate within the film using Eq. (18).
5. The flow rate calculated using Eq. (18) is then compared to the known liquid flow rate at this streamwise location found using Eq. (10)**Error! Reference source not found.**, and the liquid film cross-section is revised by decreasing film thickness δ if the liquid flow rate is overpredicted or increasing it if the flow rate is underpredicted.
6. Steps 2-5 are repeated until the calculated liquid mass flow rate matches the known flow rate. The resulting liquid-gas interface profile is then representative of the conditions at this streamwise location and the average wall heat transfer coefficient can be found by substituting Eq. (21) into Eq. (22).
7. The solution procedure is carried out from steps 1-6 at subsequent downstream computation nodes.

The present work employed a computational grid with a grid size of 1 mm in the z direction and 200 nodes in the θ direction. The number of nodes used within the channel cross-section was verified to be sufficient by doubling to 400 nodes and observing a maximum change in calculated liquid-gas interface location by only 0.14%. The iterations to find the steady solution for the liquid film cross-section in step 2 were performed until the maximum change in interface location satisfied a convergence criterion of $\left|1 - r_{i,new} / r_{i,old}\right| < 1\times10^{-7}$. The solution was considered sufficiently converged at this criterion, as further iteration to a threshold of 1×10^{-8} yielded a change in interface position of only 0.021%. The evolution step size $\Delta\eta$ used was 1×10^{-9} s and the film cross-section prediction procedure in step 6 was considered converged when the predicted streamwise liquid flow rate matched the known liquid flow rate to better than

$\left|1-\dot{m}_{f,pred} / \dot{m}_{f,\exp}\right| < 1\times10^{-3}$.

3 EXPERIMENTAL METHODS

3.1 Flow Loop

The experimental facility shown in Figure 2 contains a closed liquid-flow loop and an open air-injection loop to generate the desired adiabatic two-phase flows within the microchannel test sections. The primary liquid loop contains a gear pump (Micropump, L3467), a microturbine flow meter (Omega, FLR1009ST-D) for measuring total pump flow rate, a needle valve (Swagelok, SS-4MG-MH) for throttling flow and establishing the system pressure, and a liquid reservoir. The liquid reservoir is vented to the atmosphere and serves to separate the two-phase mixture returning from the test section. A secondary liquid loop is tapped from the primary loop immediately before the throttling valve to deliver comparatively lower liquid flow rates at a constant pressure to the single-microchannel test sections. Liquid flow to the test section is measured using a microturbine flow meter (Omega, FLR1007-D) for high flow rates from 13 mL/min to 100 mL/min, and a differential pressure flow meter (Alicat, LC-10CCM-D) for low flow rates from 0.2 mL/min to 10 mL/min. The secondary flow loop then returns the two-phase mixture exiting the test section to the reservoir for phase separation and venting. Upstream from the T-junction in the microchannel test section is the gas-handling portion of the flow loop consisting of a pressure regulator (Omega, PRG101-120) and a high-precision needle valve (McMaster-Carr, 7832K21) for controlling air flow rates. These flow rates are measured using thermal mass flow sensors specific to high (Omega, part no. FMA3105) and low (Omega, part no. FMA3102) flow rates.

The effect of volumetric void fraction α is examined in the parametric investigation of flow conditions on liquid-gas interface geometry and is calculated as

$$\alpha = \frac{j_g}{j_g + j_f}, \tag{23}$$

where j_g is the superficial gas phase velocity, and j_f is the superficial liquid phase velocity. The measurement uncertainty is ±1% of full scale (FS) for the high-end liquid flow meter and ±2% FS for the low-end liquid flow meter. The high- and low-end gas flow meters each have a measurement uncertainty of ±1.5% FS. The resulting uncertainty in void fraction over all cases considered ranges from 0.13% to 1.9% as calculated using a standard uncertainty analysis procedure [18]. The effect of Weber number is also studied to capture the relative effect of flow inertia and surface tension on the liquid-gas interface shape; the uncertainty in We for the cases investigated ranges from 2.6% to 11.1%.

3.2 Test Section

Three microchannel test sections are used for the experimental portion of the present work. Each test section comprises aluminum top and bottom clamping plates, a 1.59 mm-thick acrylic channel cover plate, and a channel block fabricated from acrylic that has a fluid inlet and outlet plenum connected by a single saw-cut microchannel of different cross-sections (160 μm × 160 μm, 510 μm × 510 μm, or 1020 μm × 1020 μm). A photograph of the D_h = 1020 μm channel block is shown in Figure 2c, along with a schematic diagram of the channel cross-section in Figure 2d. Annular flows are generated through the controlled injection of air into the single-phase liquid flow at a T-junction that is located 16 mm downstream of the channel inlet. The two-phase region of the channel is 200 hydraulic diameters in length for each test section with flow characterization being performed 100 hydraulic diameters downstream from the T-junction to ensure fully developed two-phase flow. Experimental investigations of adiabatic air-water flows in mini-scale tubes have observed two-phase hydrodynamic developing lengths of 20 diameters and suggested 100 diameters as a recommended design length [19]. Additionally, numerical simulations of mini-scale multiphase flows have demonstrated developing lengths of 40 diameters [20].

3.3 Interface Characterization

The liquid-gas interface profile is characterized across a symmetric quadrant of the channel cross-section through a tomographic approach previously demonstrated by the authors [14,21], and briefly described here. The technique leverages the relatively shallow depth-of-field of the microscope objective lenses to visualize the seeding particles within thin sections of the flow. Within each section, the seeding particles incorporated into the water are used to distinguish the liquid and gas phases. Image-processing methods developed to isolate particle location data are used to quantitatively identify the phase boundaries with an accuracy of ±4.9 μm using the 4× objective, ±2.1 μm using the 10× objective, and ±1.1 μm using the 20× objective [14,21]. By scanning across the depth of the channel, it is then possible to obtain the overall, time-averaged liquid-gas interface shape within the channel.

3.3.1 Working Fluids

The working liquid in the present experiments is water seeded with 0.5 μm-diameter fluorescent polystyrene microspheres (Magsphere Inc., PSF-500NM) at a concentration of 0.025% volume fraction; the working gas is compressed air that is filtered to remove any suspended contaminants prior to introduction into the flow loop. The particles have a peak excitation wavelength of 542 nm, a peak emission wavelength of 612 nm, and a density of 1.05

g/cm^3. At the concentration used, the presence of these particles has a negligible impact on the density, viscosity [22,23], or surface tension [24,25].

3.3.2 Illumination and Imaging

Flow visualizations are obtained using an inverted optical microscope (Nikon Eclipse Ti-U) configured to perform epifluorescent imaging whereby illumination light is delivered to the channel through the objective lens. Optimal imaging of the fluorescent signals generated by the seeding particles is achieved through the use of a custom filter cube with an excitation filter having a center wavelength of 525 nm and a full width at half maximum (FWHM) of 25 nm, a dichroic mirror with a reflection band of 525-556 nm and transmission band of 580-650 nm, and an emission filter with a center wavelength of 620 nm and FWHM of 52 nm. Excitation light is provided by a 532 nm ND:YAG laser (Quantel Brilliant Twins) pulsed at 5 ns, which eliminates any motion blur during imaging of the high-speed flows. The light energy delivered to the microscope is set to 2 mJ per pulse, as measured between the output condenser of the fiber optic coupler and the microscope body using a pyroelectric power meter. Images are recorded using a 12-bit monochrome CCD camera (Photometrics CoolSNAP HQ). The imaging sensor has an overall resolution of 1392 × 1040 pixels with a pixel pitch of 6.45 μm.

Objective lenses are chosen based on the channel size under consideration. For the largest channel size (D_h = 1020 μm) a 4× magnification lens with a numerical aperture (NA) of 0.13 is used (Nikon CFI Plan Fluor 4×). The focal plane thickness is estimated to be 39.8 μm as approximated using a formulation developed by Meinhart *et al.* [26]:

$$D_f = \frac{n\lambda}{NA^2} + \frac{ne}{M \cdot NA^2} \tag{24}$$

where n is the refractive index of the immersion fluid between the sample and the objective lens ($n = 1$ for the present study where an objective immersion oil was not used), λ is the wavelength of the light signal being observed ($\lambda \sim 620$ nm based on the filters used), and e is the minimum resolvable distance of the camera. A 10× objective lens (Nikon CFI Plan Fluor 10×) with $NA = 0.30$ and an estimated focal plane thickness of 7.1 μm was used to obtain visualizations in the intermediate channel size ($D_h = 510$ μm), while a 20× objective lens (Nikon CFI S Plan Fluor ELWD 20×, $NA = 0.45$, $D_f = 3.1$ μm) was used for the smallest channel size ($D_h = 160$ μm).

4 RESULTS

4.1 Heat Transfer Coefficient Prediction

Experimental heat transfer coefficient data were collected from studies in the literature that reported streamwise measurements of the wall heat transfer coefficient. These data were then compared against predictions obtained using the model developed in the present work. Only operating points within the annular flow regime were used for the comparison, as determined based on the microscale flow boiling transition criteria developed by Harirchian and Garimella [11], or based on flow visualizations performed in the original studies. A summary of the studies included in the comparison are provided in Table 1.

Figure 3 plots the experimentally measured heat transfer coefficient values on the horizontal axis, and predicted values on the vertical axis. In general, the model performs well with an overall MAE of 21.7% across the 251 experimental data points; 72.1% of the data points were successfully predicted within an error band of ±30%. Figure 4a plots the ratio of the predicted and measured [10] heat transfer coefficient at individual operating points as a function of vapor quality. At low vapor qualities the model consistently underpredicts heat transfer coefficient, suggesting that the predicted liquid film is thicker than the actual film. A selected data set at a fixed coolant flow rate and increasing vapor quality [10] is shown in Figure 4b with specific points of interest labelled; the liquid-gas interface at those points is plotted within the channel cross-section in Figure 4c-d. At operating point 1 the channel perimeter is fully wetted with no regions that have reached dryout; the heat transfer coefficient is underpredicted, suggesting that this film thickness is generally overpredicted in the cross section. As vapor quality is increased to operating point 2 the liquid film grows thinner with minor regions of dryout appearing along the channel perimeter. This results in a peak in the prediction, with lower predicted heat transfer coefficients at lower vapor qualities due to thicker liquid films and at higher vapor qualities due to increased regions of dryout. Between operating points 2 and 4 the prediction is dictated by the competing influences of a thinning liquid film driving the heat transfer coefficient higher, and increasingly larger regions of dryout that lower the heat transfer coefficient. Finally, at point 5, a significant portion of the channel wall is predicted to reach dryout and yields a decrease in the heat transfer coefficient.

4.2 Characterization of Liquid-Gas Interfaces

While the model benchmarking in Section 4.1 was performed against experimental heat transfer coefficient measurements across a range of channel sizes and operating conditions, detailed cross-sectional film profiles were not available for these published studies. Thus, it is difficult to precisely identify the root cause of the underprediction of heat transfer coefficient at lower vapor qualities near the onset of the annular regime. An experimental investigation was performed characterizing the liquid film cross-section to assess the model performance specific to this region. A parametric investigation of the impact of channel size and operating conditions on the interface shape during annular flow was conducted using adiabatic air-water flows. The model here is used to predict the experimentally measured interface shapes to characterize the model performance and note any trends in error that occur with decreasing void fraction. The first step was to perform a flow-regime mapping using high-speed visualizations in each of the different microchannels to determine the operating conditions necessary to obtain annular flows; the maps generated are shown in Figure 5. As can be seen, a significant portion of each flow regime map falls within the slug and annular flow regimes due to the confined nature of the flow; this confinement results from the small channel sizes under consideration coupled with a high surface tension fluid. As channel size decreases there is greater prevalence of confined flows (*i.e.*, slug and annular flows) with less of the regime map occupied by bubbly flow.

The effects of liquid and gas phase flow rates on cross-sectional interface profile are first illustrated. Figure **6**a shows experimentally measured liquid-gas interface profiles within the D_H = 510 μm test section for a fixed superficial liquid-phase velocity (j_f = 1.0 m/s) and increasing superficial gas-phase velocity (j_g = 5 m/s, 8.33 m/s, and 13.2 m/s). Interfaces are plotted with respect to the measurement domain identified within the channel cross-section shown in Figure 2d and normalized based on channel hydraulic diameter. As gas flow rate is increased, the resulting increase in interfacial shear stress drives a higher velocity liquid flow within the film, resulting in a progressively thinner film. Conversely, Figure **6**b plots the liquid-gas interface for the same test section at a fixed superficial gas-phase velocity (j_g = 8.3 m/s) and increasing superficial liquid-phase velocity (j_f = 0.33 m/s, 1.0 m/s, and 1.64 m/s). In contrast to the case with varying gas-phase superficial velocity presented in Figure **6**a, varying the liquid flow rate at a fixed gas flow rate does not affect the liquid-gas interface profile. This suggests that interfacial shear stress imparted by the vapor core on the liquid film is not the only force that drives liquid flow downstream. If only driven by interfacial shear, the liquid film thickness should increase with increasing liquid-phase superficial velocity to accommodate greater liquid flow by providing higher vapor core velocities and a larger liquid cross-sectional flow area. However, the cases presented in Figure 6b show similar interfacial shear stress conditions, as evidenced by a fixed gas-phase superficial velocity and similar vapor core geometry, which would not sustain the increasing superficial liquid-phase velocities. This experimental result is attributed to a significant contribution of capillary pumping. To better understand this behavior the relevant parameters are identified, namely void fraction, surface tension and flow inertia, and their impact is investigated.

Using the flow regime maps presented in Figure 5 four distinct void fractions ranging from 0.84 to 0.96 were chosen spanning from the lowest void fraction that yielded an annular flow to the highest void fraction that could be generated due to flow rate or pressure limitations of the facility. At each void fraction, a range of Weber number values were interrogated to observe the relative effects of flow inertia and surface tension in determining the liquid-gas interface profile within the channel cross-section; overall, a range in We from 171 to 1789 was investigated. Figure 7 shows the resulting interface measurements across the test matrix, non-dimensionalized based on the channel hydraulic diameter so that the physical measurements obtained from all three test sections can be plotted on the same axes. Also shown are the predicted interface shapes obtained using the present model. At low void fractions the liquid-gas interface recedes towards the corner of the channel with increasing We as the higher inertial forces allow the interface to recede towards the corner with higher interface curvature. This effect is diminished with increasing void fractions at which the structure of the liquid film varies minimally across the range of We values investigated. These trends are correctly predicted by the model, with larger variations in interface shape across the range of We at low void fractions, and smaller variations at high void fractions. However, discrepancies arise in direct comparison of the experimental and predicted interface profiles. As seen in Figure 7d, the model is capable of successfully predicting interface positions at a high void fraction, and has an increasing overprediction in film thickness with decreasing void fraction (Figure 7a-c). For comparison, the adiabatic void fractions considered here translate to flow qualities, x_f, of 0.006 to 0.036 where $x_f = m_g / \left(m_g + m_f\right)$. This corroborates the observations in Section 4.1, where at such low vapor qualities it is indeed an overprediction in film thickness that leads to an underprediction in the heat transfer coefficient.

The reason for the overprediction of the liquid film thickness at low void fractions can be attributed to the assumption in the model that the flow within the liquid film is purely driven by the interfacial shear stress imparted by the vapor core. The experiments here show that there is an apparent and significant contribution of capillary pumping in the liquid film at low void fractions. Despite neglecting the effects of streamwise changes in interface curvature or pressure differences between phases, model performance is not extensively impacted as was demonstrated in Section 4.1.

5 CONCLUSIONS

A novel mechanistic modeling approach for annular microchannel flows is developed that is capable of determining the liquid-gas interface shape in two dimensions within the channel cross-section by taking into account shear stress, gravity, and surface tension forces. This represents an advancement over previous models that were formulated in a single dimension by simplifying the liquid film to have a uniform thickness and considering only shear stresses. Importantly, due to the relaxed assumptions of the present model, no fitted empirical inputs are required to achieve a prediction accuracy that is comparable to previous empirically fitted mechanistic models. The model formulation is also extensible to arbitrary channel cross-section shapes. When benchmarked against 251 data points taken from the literature, the present model predicted heat transfer coefficient with an MAE of 21.7% with 72.1% of data points falling between an error band of ±30%. The heat transfer coefficient is underpredicted at low vapor qualities; however, detailed information regarding the film profile was not available in the original studies from which data was collected which could have enabled the reasons for this underprediction to be established. An experimental characterization of the film profiles in the current study revealed that the unaccounted effects of capillary pumping caused the liquid film to be overpredicted for such low flow qualities.

ACKNOWLEDGEMENTS

Financial support for this work provided by the Cooling Technologies Research Center, a National Science Foundation Industry/University Cooperative Research Center at Purdue University, is gratefully acknowledged.

REFERENCES

[1] J.E. Steinbrenner, C.H. Hidrovo, F. Wang, S. Vigneron, E.S. Lee, T.A. Kramer, C. Cheng, J.K. Eaton, K.E. Goodson. Measurement and modeling of liquid film thickness evolution in stratified two-phase microchannel flows, Applied Thermal Engineering 27 (10) (2007) 1722-1727.

[2] J. Yue, L. Luo, Y. Gonthier, G. Chen, Q. Yuan, An experimental investigation of gas-liquid two-phase flow in single microchannel contactors, Chemical Engineering Science 63 (16) (2008) 4189-4202.

[3] H. Li, P. Hrnjak, Quantification of liquid refrigerant distribution in parallel flow microchannel heat exchanger using infrared thermography, Applied Thermal Engineering 78 (2015) 410-418..

[4] S. Jesseela, C.B. Sobhan, Numerical modeling of annular flow with phase change in a microchannel, International Journal of Thermal Science 89 (2015) 87-99.

[5] S.S. Bertsch, E.A. Groll, S.V. Garimella, Review and comparative analysis of studies on saturated flow boiling in small channels, Nanoscale and Microscale Thermophysical Engineering 12 (3) (2008) 187-227.

[6] M.G. Cooper, Heat flow rates in saturated nucleate pool boiling—A wide-ranging examination using reduced properties, Advances in Heat Transfer 16 (1984) 157-239.

[7] D. Gorenflo, Pool boiling, VDI Heat Atlas, VDI-Verlag, Dusseldorf, 1993.

[8] T. Harirchian, S.V. Garimella, A comprehensive flow regime map for microchannel flow boiling with quantitative transition criteria, International Journal of Heat and Mass Transfer 53 (13) (2010) 2694-2702.

[9] W. Qu, I. Mudawar, Flow boiling heat transfer in two-phase micro-channel heat sinks—II. Annular two-phase flow model, International Journal of Heat and Mass Transfer 46 (15) (2003) 2773-2784.

[10] W. Qu, I. Mudawar, Flow boiling heat transfer in two-phase micro-channel heat sinks—I. Experimental investigation and assessment of correlation methods, International Journal of Heat and Mass Transfer 46 (15) (2003) 2755-2771.

[11] T. Harirchian, S.V. Garimella, Flow regime-based modeling of heat transfer and pressure drop in microchannel flow boiling, International Journal of Heat and Mass Transfer 55 (4) (2012) 1246-1260.

[12] T. Harirchian, S.V. Garimella, Microchannel size effects on local flow boiling heat transfer to a dielectric fluid, International Journal of Heat and Mass Transfer 51 (15) (2008) 3724-3735.

[13] T. Harirchian, S.V. Garimella, The critical role of channel cross-sectional area in microchannel flow boiling heat transfer, International Journal of Multiphase Flow 35 (10) (2009) 904-913.

[14] R.S. Patel, S.V. Garimella, Technique for quantitative mapping of three-dimensional liquid-gas phase boundaries in microchannel flows, International Journal of Multiphase Flow 62 (2014) 45-51.

[15] H.S. Wang, J.W. Rose, A theory of film condensation in horizontal noncircular section microchannels, Journal of Heat Transfer 127 (10) (2005) 1096-1106.

[16] E.O. Moeck, Annular-dispersed two-phase flow and critical heat flux, PhD Thesis, McGill University, Montreal, Canada, 1970.

[17] C.L. Ong, J.R. Thome, Macro-to-microchannel transition in two-phase flow: Part 2—Flow boiling heat transfer and critical heat flux, Experimental Thermal and Fluid Science 35 (6) (2011) 873-886.

[18] H.W. Coleman, W.G. Steele, Experimentation validation and uncertainty analysis for engineers, third ed., Wiley, Hoboken, 2009, pp. 61-81.

[19] C. Damianides, Horizontal two-phase flow of air-water mixtures in small diameter tubes and compact heat exchangers, PhD Thesis, University of Illinois, Urbana, Illinois, 1987.

[20] D. Lakehal, G. Larrignon, C. Narayanan, Computational heat transfer and two-phase flow topology in miniature tubes, Microfluidics and Nanofluidics 4 (4) (2008) 261-271.

[21] R.S. Patel, S.V. Garimella, Development of a particle tracking-based measurement technique to map three-dimensional interfaces between transparent immiscible fluids, in: Proceedings of the 13th InterSociety Conference on Thermal and Thermomechanical Phenomena in Electronic Systems, IEEE Conference Publications, San Diego, CA, 2012 pp. 1432-1437.

[22] A. Einstein, Eine neue bestimmung der moleküldimensionen, Annalen der Physik 324 (2) (1906) 289-306.

[23] R. Roscoe, The viscosity of suspensions of rigid spheres, British Journal of Applied Physics 3 (8) (1952) 267-269.

[24] T. Okubo, Surface tension of structured colloidal suspensions of polystyrene and silica spheres at the air-water interface, Journal of Colloid and Interface Science 171 (1) (1995) 55-62.

[25] B.P. Binks, Particles as surfactants—similarities and differences, Current Opinion in Colloid & Interface Science 7 (1-2) (2002) 21-41.

[26] C.D. Meinhart, S.T. Wereley, J.G. Santiago, PIV measurements of a microchannel flow, Experiments in Fluids 27 (5) (1999) 414-419.

[27] E. Sobierska, R. Kulenovic, R. Mertz, M. Groll, Experimental results of flow boiling of water in a vertical microchannel, Experimental Thermal and Fluid Science 31 (2) (2006) 111-119.

[28] P.S. Lee, S.V. Garimella, Flow boiling in a silicon microchannel array, in Proceedings of ASME 2006 International Mechanical Engineering Congress and Exposition, ASME, Chicago, IL, 2006, pp. 309-315.

APPENDIX A

The full form of the functions corresponding to the buoyancy, surface tension, streamwise pressure gradient, and interfacial shear stress terms of the mass flow rates presented in Eqs. (17) and (18) are

$$
\begin{aligned}
f_g(\delta) = -\frac{2}{3\left((r_w-\delta)^2+r_w^2\right)}\Bigg[& \frac{1}{3}(r_w-\delta)^5 - \\
& \frac{2}{3}(r_w-\delta)^3 r_w^2 + \frac{5}{12}(r_w-\delta)^2 r_w^3 - \frac{1}{12} r_w^5 + \\
& (r_w-\delta)^2\left(\frac{1}{2}r_w-\delta\right) r_w^2 \ln\left(\frac{r_w}{r_w-\delta}\right) \Bigg]
\end{aligned}
\tag{25}
$$

$$
\begin{aligned}
f_s(\delta) = -\frac{1}{2\left((r_w-\delta)^2+r_w^2\right)}\Bigg[& \frac{3}{4}(r_w-\delta)^4 - \\
& \frac{1}{2}(r_w-\delta)^2 r_w^2 - \frac{1}{4} r_w^4 + \\
& (r_w-\delta)^2 r_w^2 \ln\left(\frac{r_w}{r_w-\delta}\right)\left(2+\ln\left(\frac{r_w-\delta}{r_w}\right)\right) \Bigg]
\end{aligned}
\tag{26}
$$

$$
\begin{aligned}
f_z(\delta) = & -\frac{1}{4}(r_w-\delta)^4 \ln\left(\frac{r_w-\delta}{r_w}\right) - \\
& \frac{1}{16}\delta(\delta-2r_w)\left(3\delta^2-6\delta r_w+2r_w^2\right)
\end{aligned}
\tag{27}
$$

$$
f_\tau(\delta) = \frac{1}{4}(r_w-\delta)\left[2\ln\left(\frac{r_w-\delta}{r_w}\right)(\delta-r_w)^2-\delta^2+2\delta r_w\right] \tag{28}
$$

Table 1 Studies published in the literature from which experimental data was collected.

Study	**Channel size, material**	**Visualizations Performed**
Qu and Mudawar [10]	231 µm × 713 µm, copper	no
Sobierska *et al.* [27]	860 µm × 2000 µm, copper	yes
Lee and Garimella [28]	400 µm × 398 µm, silicon	no

List of Figures

Figure 1 Schematic diagram of annular flow morphology and cylindrical coordinate system used to model the vapor-gas interface shape within the channel cross-section (left) and a differential element in the streamwise direction (right).

Figure 2 (a) Photograph of experimental facility, (b) schematic diagram of flow loop with liquid lines shown in black and gas lines shown in red, (c) photograph of microchannel test block, and (d) schematic diagram of channel cross-section with coordinate system and measurement domain used in experimental characterization of annular flows identified.

Figure 3 Comparison of predicted heat transfer coefficient values with experimental results of (a) Sobierska *et al.* [27], (b) Lee and Garimella [28], and (c) Qu and Mudawar [10].

Figure 4 For comparison with experimental results of Qu and Mudawar [10]: (a) heat transfer coefficient prediction accuracy plotted as a function of thermodynamic vapor quality, (b) comparison to a selected test case at fixed coolant flow rate with several specific test points identified, and (c) predicted liquid-gas interface shapes plotted within channel cross-section at those points with a (d) magnified quarter-channel view.

Figure 5 Flow regime maps for (a) *Dh* = 160 µm, (b) *Dh* = 510 µm, and (c) *Dh* = 1020 µm microchannel test sections.

Figure **6** Characterization of liquid-gas interface profiles in the D_H = 510 µm test section for (a) fixed superficial liquid-phase velocity and varying superficial gas-phase velocity, and (b) fixed superficial gas-phase velocity and varying superficial liquid phase velocity.

Figure 7 Experimentally measured and predicted liquid-gas interface profiles over a range of Weber number values at four void fractions. The spatial dimensions are normalized by the respective channel hydraulic diameters for plotting of data on a single set of non-dimensional axes.

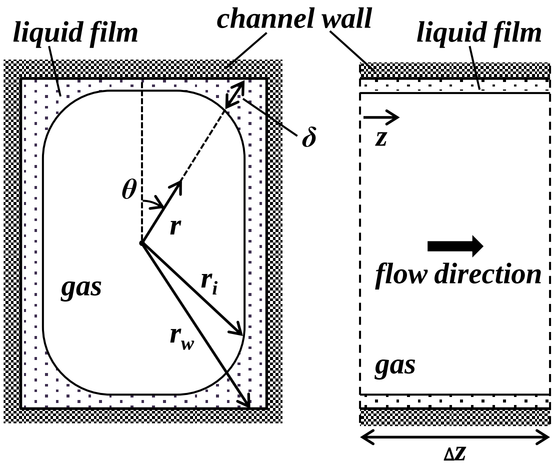

Figure 1 Schematic diagram of annular flow morphology and cylindrical coordinate system used to model the vapor-gas interface shape within the channel cross-section (left) and a differential element in the streamwise direction (right).

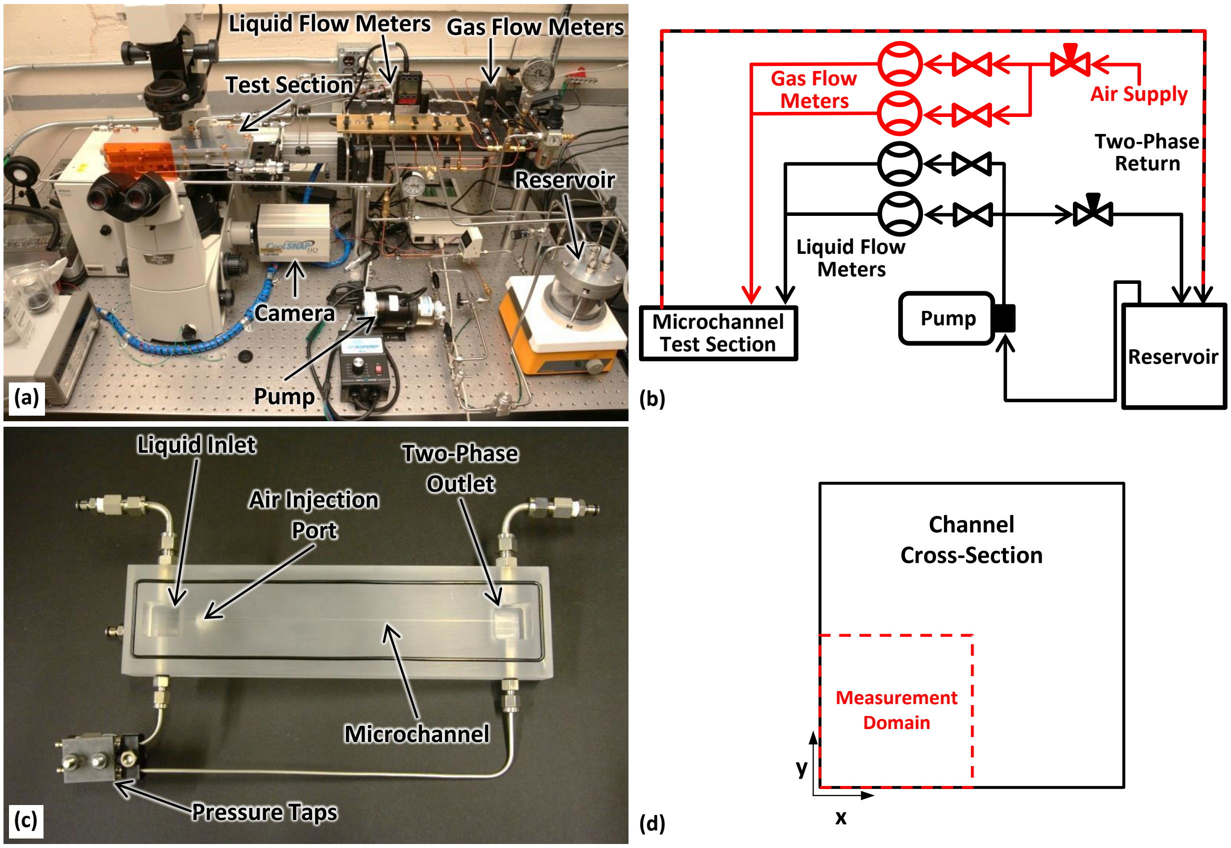

Figure 2 (a) Photograph of experimental facility, (b) schematic diagram of flow loop with liquid lines shown in black and gas lines shown in red, (c) photograph of microchannel test block, and (d) schematic diagram of channel cross-section with coordinate system and measurement domain used in experimental characterization of annular flows identified.

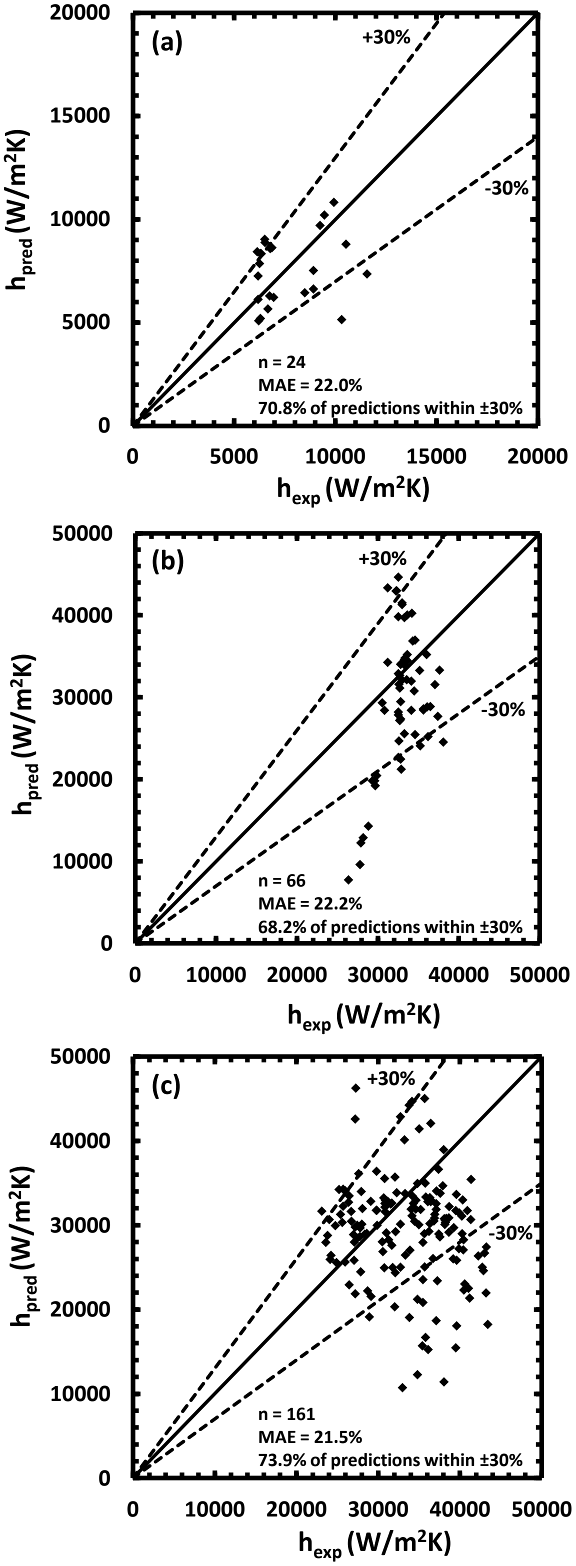

Figure 3 Comparison of predicted heat transfer coefficient values with experimental results of (a) Sobierska *et al.* [27], (b) Lee and Garimella [28], and (c) Qu and Mudawar [10].

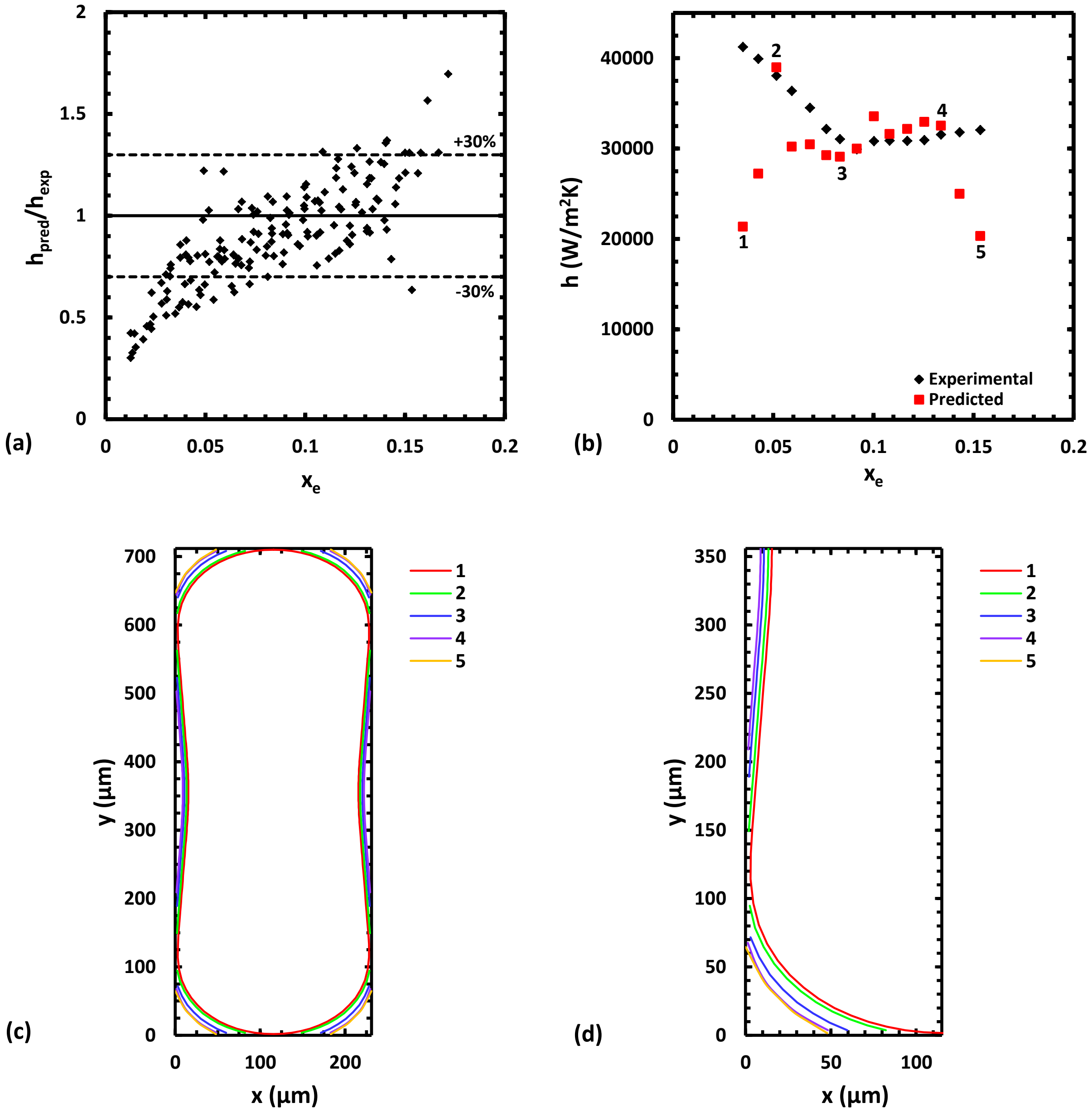

Figure 4 For comparison with experimental results of Qu and Mudawar [10]: (a) heat transfer coefficient prediction accuracy plotted as a function of thermodynamic vapor quality, (b) comparison to a selected test case at fixed coolant flow rate with several specific test points identified, and (c) predicted liquid-gas interface shapes plotted within channel cross-section at those points with a (d) magnified quarter-channel view.

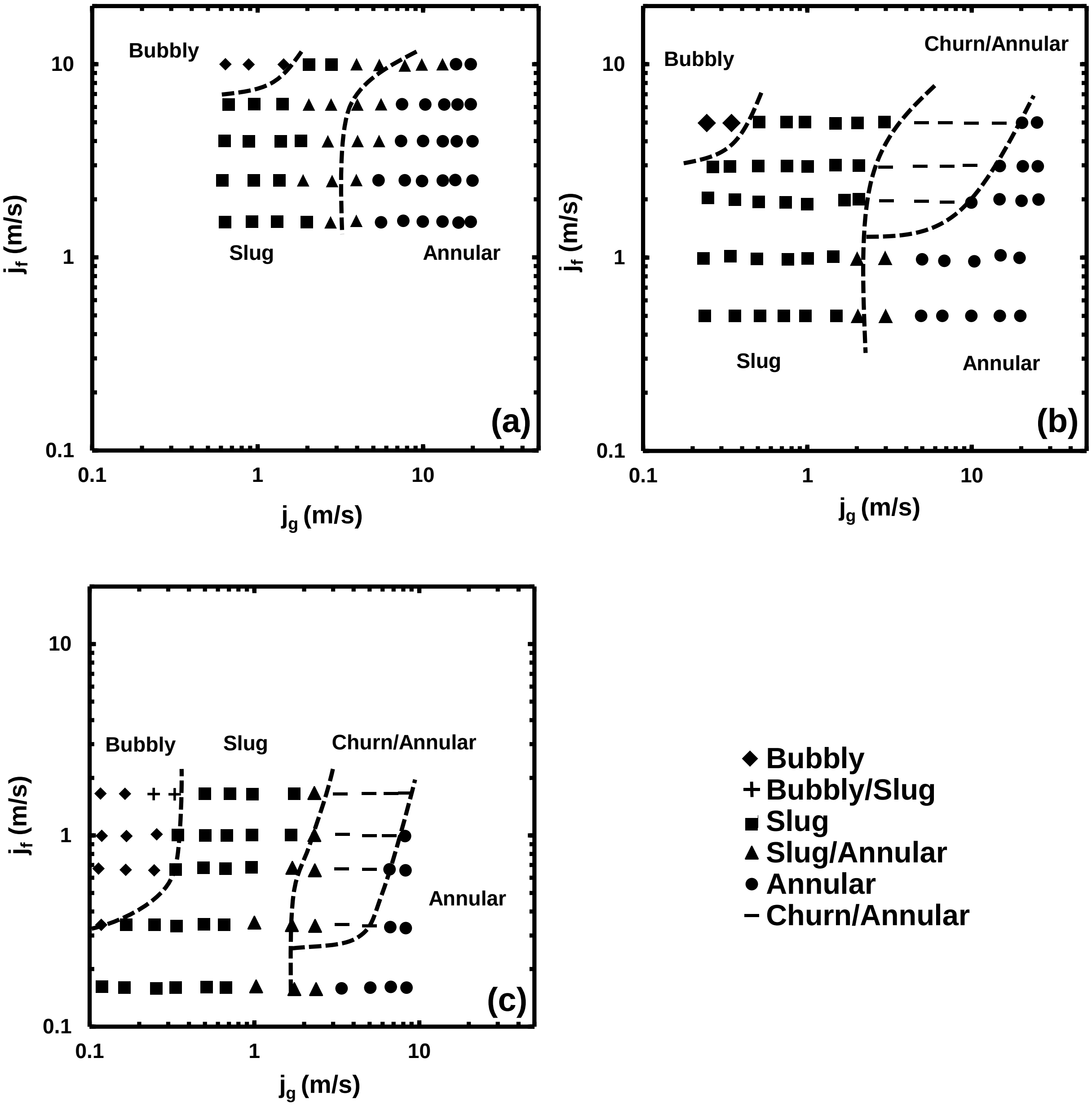

Figure 5 Flow regime maps for (a) D_h = 160 µm, (b) D_h = 510 µm, and (c) D_h = 1020 µm microchannel test sections.

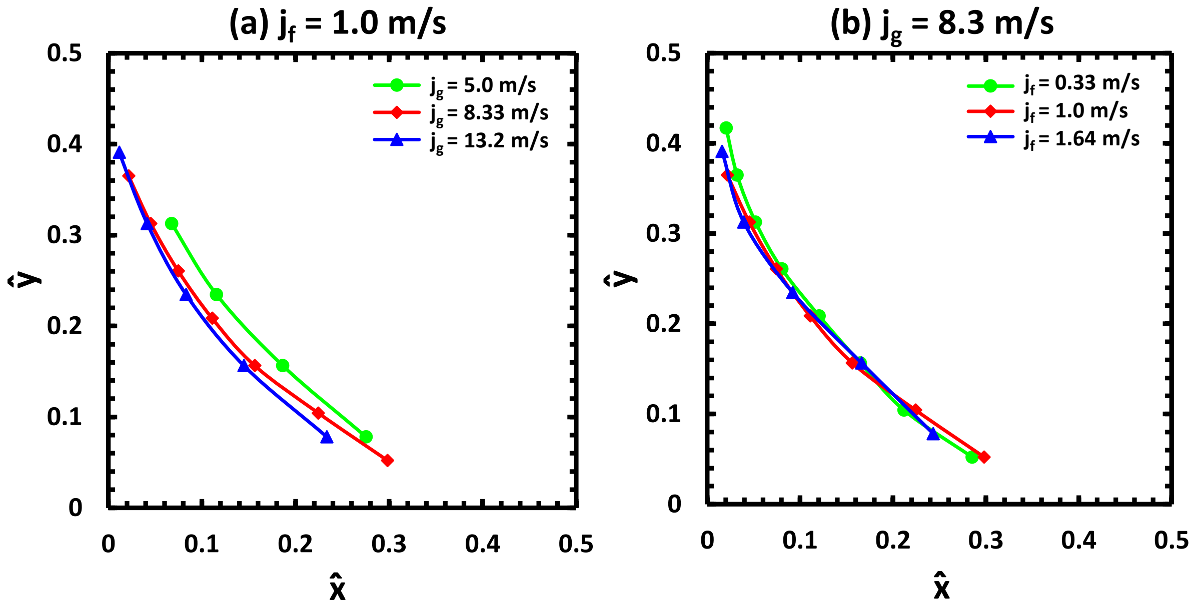

Figure 6 Characterization of liquid-gas interface profiles in the D_H = 510 µm test section for (a) fixed superficial liquid-phase velocity and varying superficial gas-phase velocity, and (b) fixed superficial gas-phase velocity and varying superficial liquid phase velocity.

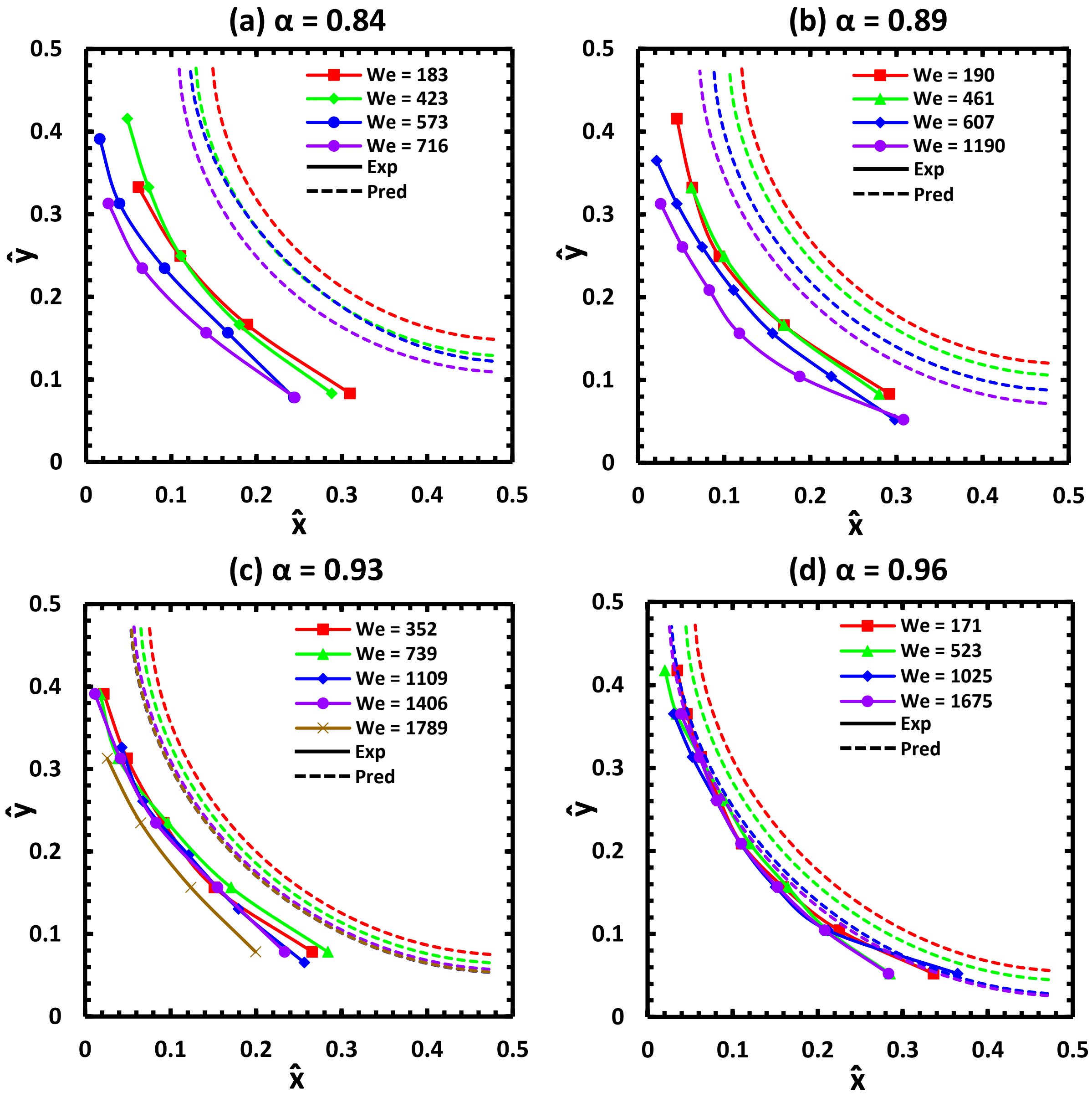

Figure 7 Experimentally measured and predicted liquid-gas interface profiles over a range of Weber number values at four void fractions. The spatial dimensions are normalized by the respective channel hydraulic diameters for plotting of data on a single set of non-dimensional axes.